Variability Aspects of the Mars Surface Data from Summer to Winter Solstice: Viking Lander 1 Observations Revisited

5 authors, including:

Mariza Pereira de Souza Echer
National Institute for Space Research, Brazil
76 PUBLICATIONS **456** CITATIONS

SEE PROFILE

Margarete O. Domingues
National Institute for Space Research, Brazil
155 PUBLICATIONS **614** CITATIONS

SEE PROFILE

Odim Mendes
National Institute for Space Research, Brazil
146 PUBLICATIONS **610** CITATIONS

SEE PROFILE

E. Echer
National Institute for Space Research, Brazil
361 PUBLICATIONS **3,174** CITATIONS

SEE PROFILE

Some of the authors of this publication are also working on these related projects:

Adaptive Multirresolution View project

MHD in Space Sciences View project

Variability Aspects of the Mars Surface Data from Summer to Winter Solstice: Viking Lander 1 Observations Revisited

Mariza Pereira de Souza Echer, Margarete Oliveira Domingues, Odim Mendes, Ezequiel Echer & Walter Gonzalez

Volume 43 • Number 4

Brazilian

Journal
of
Physics

ONLINE
FIRST

Springer
ISSN 0103-9733 • 13538
43(4) 209–294 (2013)

SBF
SOCIEDADE BRASILEIRA DE FÍSICA

Available online
www.springerlink.com

Springer

Springer

SBF
SOCIEDADE BRASILEIRA DE FÍSICA

GENERAL AND APPLIED PHYSICS

CrossMark

Variability Aspects of the Mars Surface Data from Summer to Winter Solstice: Viking Lander 1 Observations Revisited

Mariza Pereira de Souza Echer[1] · Margarete Oliveira Domingues[1] · Odim Mendes[1] · Ezequiel Echer[1] · Walter Gonzalez[1]

Abstract
In this work, we revisited the meteorological datasets of temperature and pressure, recorded onboard the Viking Lander 1, evolving from summer to winter Martian solstice. The datasets were provided by the Viking Meteorology Experiment Team and we performed the study using a multiscale signal analysis technique based on an available wavelet transform methodology. Even in the presence of data gaps, the methodology provides the skill to perform the time-scale signal characterization. We highlighted the results with new features related to the non-stationary behavior in the data. The main spectral periods found in pressure data are 0.25 SOL (6.25 h), 0.33 SOL (8.3 h), 0.5 SOL (12.5 h), 1 SOL (25 h), 10.2 SOLS, a broad peak between 21 and 33 SOLS. In temperature, the main periods were 0.5 SOL (12.5 h), 1 SOL (25 h), and 32 and 64 SOLS. The correlation between the pressure and temperature data shows anti-correlation in the scales larger than 1.5 SOL, with a high determination coefficient (more than 64%).

1 Introduction

The space age had its beginning in 1957 with the success of the Sputnik satellite launch. The world was engaged in a kind of space race, where the protagonists were the USA and the Soviet Union. The Soviet spacecraft Luna 9 (1966) was the first robotic mission to perform the soft landing on the moon. The Americans sent the manned Apollo 11 to the moon 3 years later (1969). The Soviets sent Venera 7 (1970) to Venus. It was the first robotic mission to land on another planet, and from there, it transmitted data to Earth for almost 1 h. Knowledge about our solar system has increased rapidly. Nowadays, we can observe and probe the Sun and the inner and outer planets.

The fourth planet from the Sun (an inner planet), named as Mars after the Roman God of war, has been visited over last decades by several space missions. Among them for instance, some missions that encountered and probed the planet were, as flyby or as orbiter, land and rover, the Mariner 4 (1964), Mariners 6 and 7 (1969), Mariner 9 (1971), Vikings 1 and 2 (1975), Mars Global Surveyor – MGS (1996), Spirit and Opportunity (2004), Mars Express (2003), Mars Reconnaissance Orbiter (2005), Mars Science Laboratory (2011), and Mars Atmospheric and Volatile EvolutioN—MAVEN (2013).

Those missions have shown us that Mars is a rocky, cold, and dry planet. The planet mean diameter is 6,779 km, it has an eccentric orbit, and it presents an obliquity of 25.2°. The mass is 6.42×10^{23} kg. It has two small satellites, Phobos (size $27 \times 22 \times 18$ km), and Deimos (size $15 \times 12 \times 10$ km) [6].

Mars is the most accessible planet for us in the solar system, in an orbit of approximately 228×10^6 km from the Sun, practically very close the Earth's orbit. Comparatively,

✉ Mariza Pereira de Souza Echer
mariza.echer@inpe.br

Margarete Oliveira Domingues
margarete.domingues@inpe.br

Odim Mendes
odim.mendes@inpe.br

Ezequiel Echer
ezequiel.echer@inpe.br

Walter Gonzalez
walter.gonzalez@inpe.br

1 National Institute For Space Research (INPE), São José dos Campos, Brazil

Springer

both planets have some similarities. From the space to ground, all probes have observed in rich details from the upper atmosphere to the Martian surface. However, those missions tell us that the vertical temperature profile of the Martian atmosphere is entirely different from that of the Earth's atmosphere. Partly, this difference is caused by the lack of ozone to create a stable stratosphere and partly by the effects of dust [21]. Usually, in the lower part of the atmosphere, the temperature decreases with the elevation as in the Earth's troposphere. Up to 45 km, the temperature is controlled mainly by exchange of heat with the ground (latent heating is negligible here due to small amounts of water present). From 45- to 110-km elevation, the temperature continues to decrease; however, radiative emission and absorption by CO_2 dominate. Above 110 km (mesopause region), due to absorption of extreme ultraviolet radiation, the temperature gradient becomes reverse, like at Earth's atmosphere [4]. Above the mesopause, at 125 km, is the homopause, a region of Martian atmosphere where gases begin to separate diffusively. At still higher elevations is the exosphere, the region where the atoms and molecules are on ballistic trajectories and can escape to space.

At the Martian surface, according to Forget et al. [6], in some places, such as in tropical latitudes, there is a regime of trade and monsoon winds rather like those on Earth. On Mars, the diurnal oscillation of winds is a significant phenomenon because of the differences between daytime and nightime temperatures. During the nights, the thin atmosphere, composed mostly of CO_2, near the Martian surface, with temperatures around $-65\ °C$, becomes extremely cold. As a consequence, the Martian atmosphere as a denser gas tends to flow, running down slopes and creating strong localized winds until the sunrise. In the afternoon, the opposite occurs, as warmer air near the surface goes up slopes. The Martian atmosphere vibrates and transmits diurnal and semi-diurnal frequency waves [6]

The circulation of the Mars atmosphere has several components [22]. According to Zurek [22], a north-south flow (meridional flux) results from a seasonal exchange of CO_2 between the two poles. Meridional flux and strong latitudinal thermal gradients in the winter hemisphere cause instabilities (eddies) at mid-latitudes. As a consequence, eastward-propagating planetary waves develop, and they are followed by strong westerly winds, high-altitude jet streams and travelling storm systems.

Carr [4] mentions that heating of the atmosphere at low and mid-latitudes in the summer hemisphere causes air to rise and promotes a seasonal meridional overturning, like a Hadley cell, which extends across the equator. This is also a natural mechanism facilitating the exchange of water vapor between the two hemispheres. Other elements of the circulation include low-latitude westward-propagation thermal tides, driven by diurnal heating cycles, and also

quasi-stationary waves caused by large-scale topography and variations in albedo.

The previous and recent Mars missions provide precious opportunities to answer questions about the formation and the early evolution of the planet, and climate processes that have shaped the planet through the times, in a specific sense, how Mars compares to and contrasts with Earth.

The purpose of this work is to revisit the meteorological datasets, onboard the Viking Lander 1 (VL–1), from summer to winter solstice at the surface, the same period studied by Ryan et al. [17]. The VL–1 meteorological sample was provided by the Viking Meteorology Experiment Team and downloaded from Planetary Data System. Generally, the data sample revisited in this work was used by several groups and the papers depict different approaches to the planet Mars, as well as the sample serves as ground truth for comparison with proposed theoretical approach, as we can see by Tillman et al., Hess et al., Ryan et al., Snyder [11–13, 17–19].

In this work, we are using this time a multiscale signal analysis technique based on wavelet transform. Here, the purpose is to highlight the results with new features related to the non-stationary behavior of these datasets. We present the contents as follows. In Section 2, we present the datasets to be analyzed. In Section 3, we establish the methodology for the treatment of the data. In Section 4, we present and discuss the results obtained. In the last section, we summarize the work and present the final remarks.

2 Martian Site and Dataset

Historically, the Viking mission represents an achievement for humanity in many aspects. It was not the first time that we touched down one extraterrestrial surface. However, we landed a spacecraft safely outside our planet and made the direct acquisition of data during a long period. The Viking Lander I (VL–1) touched down on the western slope of Chryse Planitia (the Plains of Gold), which is at 22° N, 48° W, a region that can be categorized as a tropical site, on July 20, 1976.

Mars is a terrestrial planet, and it has an obliquity close to the obliquity of Earth (23.4°), but has a more eccentric and longer orbit when compared to Earth, presenting the year with rounded 669 SOLS. SOL is a word designated to the Martian day that lasts 24 h 39 min 32.25 s ($\sim$ 25 h). The SOLS are measured from the time of the VL–1 landing.

Immediately after the summer solstice for the northern hemisphere, VL–1 touched down safely on Martian surface and started to probe its extreme environments. The site on the surface was seen as a sparsely cratered hemisphere of Mars, and their surroundings look barren, rock-strewn deserts as described by [4, 11–13, 16]. At the surface, CO_2

composes more than 95% of the atmosphere for most of the year; nitrogen (N) at 2.7% and argon (Ar) at 1.6%, and $\sim$ 1% are the other constituents as oxygen (O), carbon monoxide (CO), neon (Ne), krypton (Kr), xenon (Xe), and ozone (O_3). The proportion of water vapor is variable. During the summer in the lower atmosphere, it could reach several percents. However, in winter, it may be 1 ppm [18].

In our analyses, we revisited the data of temperature and pressure from VL–1, which includes $\sim$ 350 SOLS [18, 19] recovered with a resolution of 0.04 SOL. The measurements of temperature were made by VL–1 at 1.5 m above the Mars surface. The sample data is divided into two intervals, the first one from SOL 1 up to SOL 116.98, and the second from SOL 134.02 to SOL 350.98 (taking into account the data gap).

According to Hess et al. [14], the pressure on Mars obtained by VL–1 shows three different types of fluctuations caused by different physical processes. The first one is a daily variation consisting primarily of diurnal and semidiurnal thermal tides. The second is a fluctuation from SOL to SOL produced by travelling meteorological disturbances (these have periods of several SOLS). The third type is the extended period of fluctuations, which is dominated by annual and semi-annual components, caused by seasonal condensation and evaporation of CO_2, the main atmospheric constituent, to and from the polar caps [13, 17, 19]. Mars is unique in that almost 25% of its atmosphere cycles in and out of carbon dioxide ice polar caps each year [1]. Figure 1, as a visualization example, presents the pressure and temperature data for SOL 80 (the top panel) and 250 (the bottom panel), where it is possible to see the diurnal and semi-diurnal variations.

3 Methodology

We use in our analysis the continuous wavelet transform (CWT) to investigate the variability of pressure and temperature data at the surface of Mars. The wavelet technique has the skill to present the scale-time representation of a signal. The CWT is defined as a convolution of the signal $s(t)$ that represents the data with the analyzing wavelet function $\psi(t)$,

$$W_s^{\psi}(a, \tau) = \frac{1}{\sqrt{a}} \int s(t) \, \overline{\psi\left(\frac{t-\tau}{a}\right)} dt, \qquad (1)$$

where the over-line symbol denotes the complex conjugate, the $W_f^{\psi}(a, \tau)$ are the wavelet coefficients, and a and τ are the scale and translation in time parameters, respectively. Practically, with the numerical implementation, we choose appropriate ranges and variations of the scale and translation parameters. Geometrically, the scale parameter produces contraction or dilation of the analyzing wavelet function ψ around the translation parameter τ. The variations of these parameters provide the multiscale aspects of the wavelet transform. A review of that transform can be found in the textbook [2]. The square of the moduli of these coefficients is interpreted as the signal energy present in the time τ and scale a, if we consider the value $\frac{1}{\sqrt{a}}$ as the normalization constant in the integral transform (as we used in Eq. 1). Using this choice, we ensure the energy conservation between the time and the scale domains. The term energy is used here in the mathematical context of the space of square integrable functions on $\mathbb{R}$ that is an analogy of kinetic energy in physics context [2]. Therefore, this normalization guaranties the energy conservation similarly as the Parseval's theorem for Fourier transform. The constant $\frac{1}{\sqrt{a}}$ is used to ensure the energy conservation between time and frequency domains.

The square of the moduli of these wavelet coefficients is usually arranged in a two-dimensional array of size $a \times \tau$
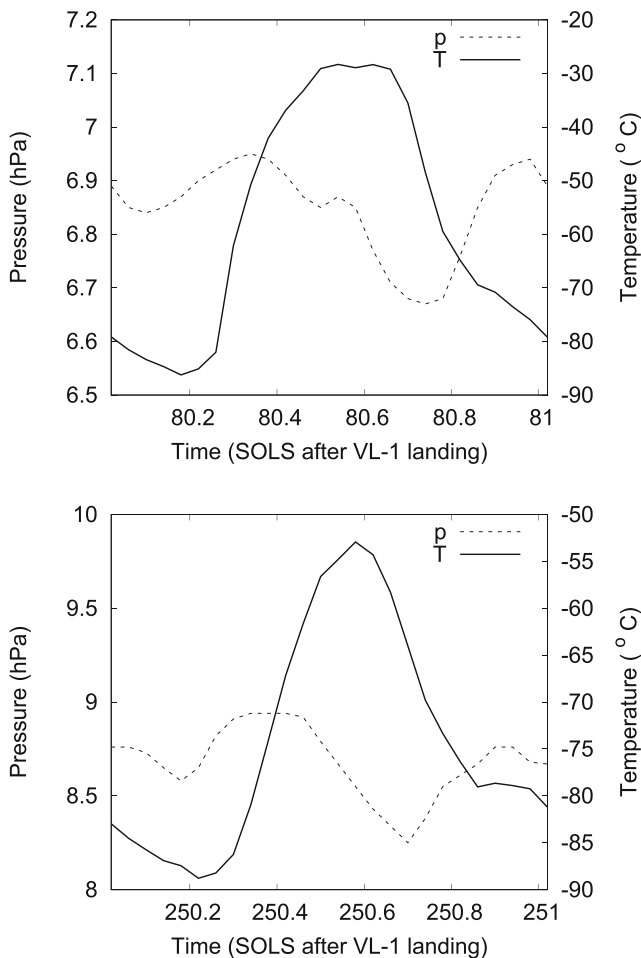
Fig. 1 Example of surface pressure (dashed line) and temperature (solid line) recorded by the VL–1 land. Two time intervals of one SOL (i.e., Martian day) are presented

and is interpreted as the energy present in each time τ and scale a. Therefore, we consider

$$E_s^\psi(a, \tau) = |\mathcal{W}_s^\psi(a, \tau)|^2, \tag{2}$$

that is a local measure of the energy present in the signal s in the time-scale plane and is called scalogram. Interpreting the scalogram by an appropriate color palette allows the detection of sudden changes in the signal behavior, as time discontinuities or period band changes versus time. Its reading identifies the moments when these phenomena occur because these region readings of wavelet coefficients indicate higher values of energy.

The distribution of energy in the time-scale plane is different for each choice of wavelet function ψ.

In analogy with the Fourier spectrum, the global wavelet spectrum is defined by

$$\mathbb{S}_s(a) = \int_{-\infty}^{\infty} E_s^\psi(a, \tau)\, d\tau, \tag{3}$$

and it can be interpreted as the distribution of energy present for their scales. In practice, it provides a smooth version of the Fourier spectrum for periodic signals [9].

To avoid the side effects of the gaps on the dataset, we used the gapped wavelet transform described in [9]. The main idea of this approach is to restore the admissibility condition near the gaps, and moreover to improve the accuracy of frequency band determination of short signals. Basically, the analyzing wavelet is separated in an oscillatory and an envelop part leading to a new wavelet function locally when it is necessary. In this version of the CWT, the wavelet analyzing function is given by,

$$\psi_{\text{gap}}(t, a, \tau) = \frac{1}{\sqrt{a}} \psi\left(\frac{t - \tau}{a}\right) G(t), \tag{4}$$

where $G(t)$ is the transfer function for the data gaps. $G(t)$ is chosen as one if the signal is correctly registered and zero otherwise, and ψ is the complex Morlet wavelet defined by

$$\psi(t) = \exp(-\iota\, 6\, t)\, \exp\left(\frac{-t^2}{2}\right).$$

In this case, scale and time bands are in equilibrium according to the Heisenberg uncertainty principle [2, 5]. This modified Morlet wavelet leads to an adaptive wavelet expressed by

$$\psi'(t, a, \tau) = \left[\exp(\iota\, 6\, (t - \tau)) - \mathbb{K}(a, \tau)\right]$$
$$* \exp\left(\frac{-(t - \tau)^2}{2}\right) G(t), \tag{5}$$

where

$$\mathbb{K}(a, \tau) = \left[\int \exp\left(\frac{-(t - \tau)^2}{2}\right) G(t)\, dt\right]^{-1}$$
$$\times \left[\int \exp(\iota\, 6\, (t - \tau)) \exp\left(\frac{-(t - \tau)^2}{2}\right) G(t)\, dt\right].$$

These changes in the CWT guarantee that near the gaps, ψ_{gap} is used instead of ψ_{Morlet} and ensure to restore the admissibility condition by repairing it in some way through the wavelet function itself. In this case, the scale is directly related to the pseudo-period (also called central period), and consequently, it is the inverse of the pseudo-frequency (also called central frequency).

In a complementary approach, wavelet cross-correlation analysis allows us to verify the interaction between pressure (p) and temperature (T) for each considered scale (more details in [8]). In practice, it is computed after we obtain the wavelet transform from Eq. 1 as

$$\mathcal{C}(a) = \frac{\int W_{s_1}(a, \tau)\, \overline{W_{s_2}(a, \tau)}\, d\tau}{\sqrt{\mathbb{S}_{s_1}(a)\, \mathbb{S}_{s_2}(a)}}, \tag{6}$$

where $W_s(a, \tau) = |\mathcal{W}_s^\psi(a, \tau)| - |\widetilde{\mathcal{W}_s^\psi(a, \tau)}|$, with the tilde symbol indicating the arithmetic mean over all times τ, and s_1 and s_2 refer to the considered signals. Based on this complex measure $\mathcal{C}(a)$, we compute the correlation modulus and phase concerning each scale a. This correlation modulus varies from zero to one, and the correlation phase from zero to 2π.

Following, the data analysis is presented. On the performed wavelet analysis, we use the normalized anomaly series. We remove the mean value of the series and divide by its standard deviation. These values of mean and standard deviation are $\{7.78, 0.81\}$ hPa, for pressure, and $\{-65, 87, 19.61\}$ ^{o}C, for temperature, respectively. Therefore, the normalized anomaly series have zero mean and standard deviation one. On the series, there are 408 consecutive gaps, from days 116.98 to 134.02. Then, there is a total of 408 missing data in the total of 8733. The gap wavelet here is used to avoid undesired effects in the analysis near the large gap, and the non-periodic interval related to the time series. It is worthwhile to note that inevitably border distortions occur in CWT, as in many other integral transforms, when applied to a finite length time series (similarly, the series analyzed here); this is due to the fact that the values of the transform at the beginning and the end of the time series (the same for the borders of gaps) are always not well correctly computed, in the sense that they involve missing values of the series which are then artificially prescribed. Nevertheless, these effects are not significant in the current analysis because of the gap CWT approach used here, as discussed in [7, 9]. It is a natural improvement in the CWT for practical applications [8, 15]. Therefore, it is not necessary to apply the cone of influence on the scalograms to avoid side effects; however, bias effects could still be present.

Considering the wavelet coefficients $\mathcal{W}_s^\psi(a, \tau)$, herein, we denote $s = p$, in reference of the pressure data, and $s = T$, for temperature data. A similar notation is used

in the wavelet cross-correlation part, where $s_1 = p$ and $s_2 = T$. We are interested in the correlation phases near zero (or 2π), or near π, i.e., the ones related to phase or anti-phase in respect to the considered scale, respectively. The values of these phases only make sense where we also have significant values in the correlation modulus (usually larger than 0.7, i.e., with a determination value corresponding to 49%).

4 Results and Discussions

The main results concerning the VL–1 temperature and pressure data analysis are presented as follows. The features identified with the wavelet methodology are discussed.

Figure 2 shows the sample of the temperature time series, in Celsius degrees, of the VL–1 (at the top panel). Following the sequence of presentation of the results, we observe the scalogram, which is a Gray-scale map containing the period bands detected with the CWT (bottom-left panel), and the global wavelet spectrum (bottom-right panel) for the anomaly series.

From Fig. 2 (top panel), we observe the temperature dataset. It started to be recorded just after the summer solstice (solar longitude 90) for the northern hemisphere. Apparently, for this time interval of the Martian year, the weather seems to present more regular behavior at the northern hemisphere. As we can see, the temperature (top panel) presents from SOL 1 up to 215 a large dispersion, which shows the characteristics for the Martian summer, with high fluctuations due to the maximum during daytime and minimum values detected during the night. From SOL 215 to SOL 315, we can see a very slight decrease and less dispersion, as a consequence of the transition from autumn to winter. We note a decrease in the amplitude of fluctuations of the maximum and minimum

values of temperature. After SOL 315, we observe lower dispersion, related to winter, when there are no large differences between the maximum and minimum values for temperature. It is possible to notice that the daily maximum temperature also decreases from the summer (SOL 1) up to winter (SOL 350) at the northern hemisphere. It is known in general that the temperature on the surface of Mars shows a homogeneous behavior. It is more stable throughout the Martian year (long period). However, the temperature has significant fluctuations and can change rapidly in response to diurnal cycle—short periods (as seen in Fig. 1 for SOL 80 and SOL 250). The MGS mission reported that the thin atmosphere could change rapidly from dusty and warm to translucid and cold conditions. However, previously (1975), the Viking Lander data observations had demonstrated that even the most translucent Martian atmosphere contains significant quantities of aerosols-dust. The solar radiation absorption by dust may be the main cause for the lower atmosphere to be more stable, as proposed by Albee et al.[1].

In Fig. 2 (bottom-left panel), we can see the scalogram for temperature. We use a log-two representation for the energy. It is seen a Gray-scale map with four tones that are associated with the scale (period band or central period) characteristics given in terms of the intensity of the scale (i.e., described by the amount of the relative signal energy). The Gray-level change indicates less (dark-gray tone) or more (light tone) energy involved in $\log_2$ representation. The white rectangle indicates the large data gap that we did not treat.

Perceptible regions are associated with short periods, diurnal (1 SOL) and semi-diurnal (0.5 SOL), especially after SOL 200. Moreover, the energy associated to scale four can be seen at a spectral peak in the wavelet spectrum due to its contribution after SOL $\sim$ 150. It is also possible to see a variation in scale 2 to 16 SOLS on the Gray-scale map immediately after the data gap (SOL $\sim$ 200) compared

Fig. 2 Temperature time series (°C) of VL–1 mission (top panel). Scalogram (bottom-left panel) and the global wavelet spectrum (bottom-right panel) are related to the normalized temperature. Gaps are due to lost data
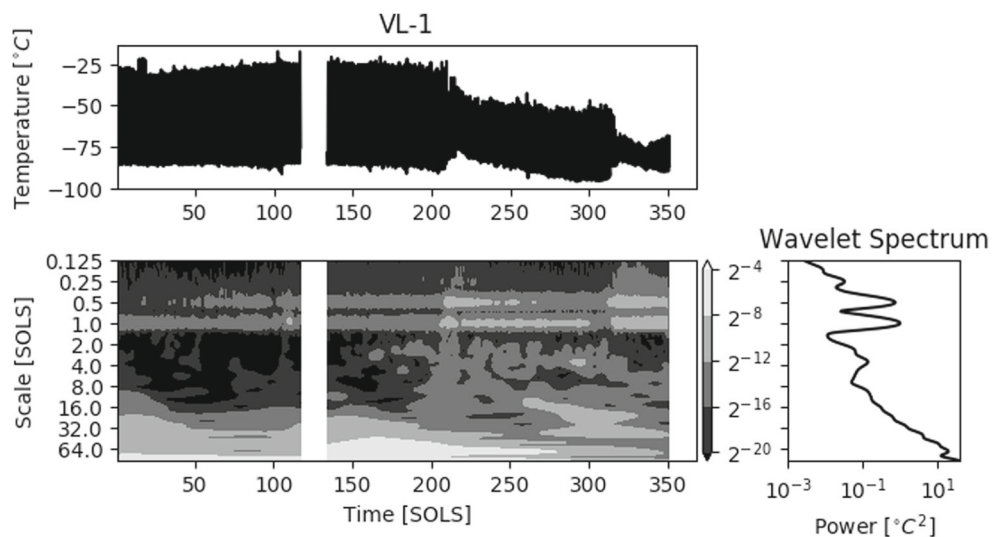
to the period before. This Gray region spreads anisotropically, involving all period bands. It is possible that this change in temperature behavior is associated with seasonal variation. Even more, long periods, 32 SOLS and 64 SOLS are highlighted and continued throughout the data period for temperature.

The last plot in Fig. 2 (bottom-right panel) is the global wavelet spectrum. It is possible to see the energy of the diurnal and semi-diurnal variations, and also we can see a contribution in the scale between two and four SOLS. However, the contribution of the latter scales is concentrated in a short period of time SOLS $\sim 150 - 320$.

Due to the sample size, its length having approximately half a Martian year, we only indicate here the presence of the long period fluctuations (32 and 64 SOLS)—those periods with larger scales and apparently with strong energy.

In addition to daily temperature fluctuations, another component that influences the surface temperature is the latitude. Due to the obliquity of the planet, the Martian temperature has latitudinal dependence which leads Mars to receive more heating at the surface in the tropics than in the poles. The resulting temperature gradient produces a pressure gradient that drives a north-south (meridional) circulation.

Figure 3 shows the VL–1 pressure time series, using the same layout as seen in Fig. 2. From Fig. 3, we can see pressure in hectopascals (at the top panel), scalogram (bottom-left panel), and the global wavelet spectrum (bottom-right panel). In the scalogram, it is seen a Grayscale map with three tones, and the change indicates less (in this case dark-gray tone) or more (light tone) energy involved represented in $\log_2$ representation.

Figure 3 (top panel) shows the fluctuations from SOL to SOL of the daily average pressure at the end of summer close to ~ 6.8 hPa (minimum) and its increase during the passing of the season when in the fall equinox CO_2 ice

begins to sublimate (solar longitude 180, $\sim$ SOL 150) up to winter solstice at northern hemisphere (solar longitude ~ 270, SOL 300).

Mars has a more eccentric and more extended orbit than Earth, which means that seasons develop under different duration and intensity. The southern spring and summer are short and hot, and the fall and winter are long and cold. During perihelion, the closest point between Sun and Mars, which occurs during the winter solstice in the northern hemisphere, Mars is 20% closer to the Sun than during aphelion. In this orbital position, the planet receives almost 40% more solar energy [1], and the atmospheric trapped (CO_2) during the southern winter in the polar ice cap sublimates and it is released, thus closing the atmospheric cycle. It is possible to see in Fig. 3 (top panel) that the maximum average value of atmospheric pressure is 9.5 hPa. The perihelion is also a period where dust storms occur due to the release of the atmosphere trapped in that polar cap. As a result, an intensification occurs in the regime of the winds and the global circulation [10]. According to Barlow [3] the generation of the winds on Mars is linked directly to the atmospheric pressure and temperature gradients. These gradients result from three major factors: seasonal changes, dust storms, and diurnal variation. The first factor is the seasonal change which results from condensation and sublimation of CO_2 and H_2O from the polar caps. The second, as we noted before, are dust storms that can enhance the temperature gradient, the variation produced leading to strong winds. The last major factor is the diurnal variation resulting from the temperature differences between the day and night sides of the Mars and the presence of passing storm systems.

From the scalogram in Fig. 3 (bottom-left panel), the main spectral central periods found in pressure data are 0.25 SOL (6.25 h), 0.33 SOL (8.3 h), 0.5 SOL (12.5 h), 1

Fig. 3 Pressure time series (hPa) of VL–1 mission (top panel). Scalogram (bottom-left panel) and the global wavelet spectrum (bottom-right panel) are related to the normalized pressure. Gaps are due to lost data
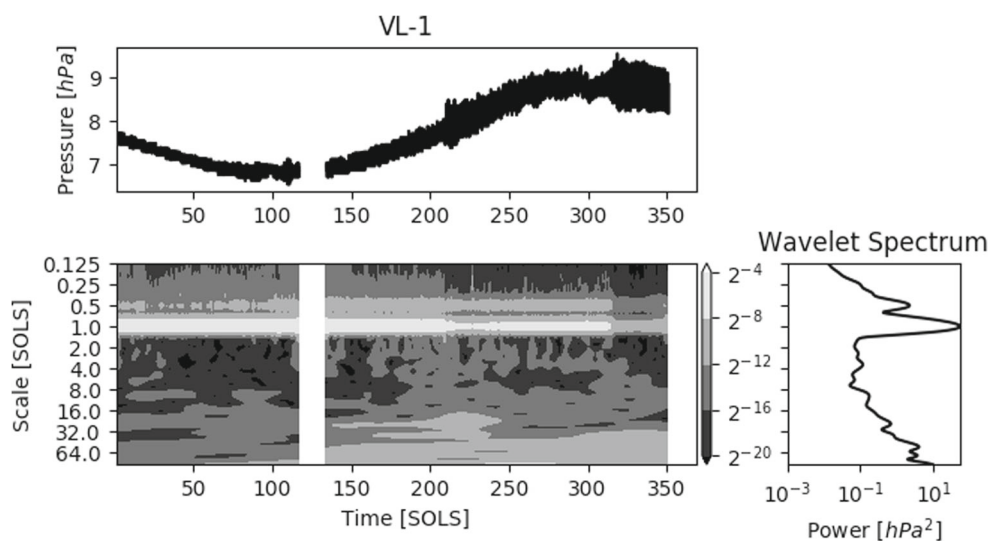
SOL (25 h), 10.2 SOLS, a broad peak between 21 and 33 SOLS, and another at the range 32–64 SOLS. Noticing the main central periods of 0.5 SOL and 1 SOL, we attributed these periods to semi-diurnal and diurnal oscillations that consist in increased heating through absorption of solar radiation by dust and an associated increase in the amplitude of the semi-diurnal and diurnal pressure tides, which is the daytime (1 SOL) cycle of temperature and pressure on Mars [14]. Therefore, as the site where VL–1 landed is a tropical latitude, the atmospheric pressure response to solar heating is much more prominent. The central period of approximately 10 SOLS seems to be related to planetary pressure wave events [18]. The broad peak between 20 and 33 SOLS might correspond to the frequency of the 26-day solar rotation signal recorded in the surface data [17, 19, 20].

In Fig. 3, by global examining the wavelet spectrum (bottom-right panel), we can see a well-defined diurnal and semi-diurnal cycle (near 1 SOL scale and 0.5 SOL scale, respectively). Therefore, we point out that diurnal and semi-diurnal cycles are well defined in both pressure and temperature wavelet spectra (Figs. 2 and 3 bottom-right panel). However, there is a seasonality variability in the energy contributions for these scales as presented in their scalograms (Figs. 2 and 3 bottom-left panel). It is worthwhile to mention that in the pressure data, diurnal cycles are strongly defined before time ≈ 200, and weaker after 330. Scales with $2 - 8$ SOLS seem to be present only in the pressure data from $100 - 330$ SOLS.

Tillman et al. [19] reported the occurrence of a large increase in the daily average pressure detected by VL–1 between SOLS 209 and 210, corresponding to the Lander 1 pressure jump. Hess et al. (1980) signalled for SOL ≈ 200 and 300 the occurrence of global dust storms [14]. It was a clear demonstration of the power that the first global dust storm had.

Ryan et al. [17] observed that atmospheric pressure had a significant diurnal and semi-diurnal oscillation driven by diurnal heating. They pointed that as the season progressed, the diurnal and semi-diurnal oscillation in pressure and also in wind increased in parallel with atmospheric opacity. They also observed that diurnal temperature variation appeared to be controlled directly by atmospheric opacity. In other words, opacity increases and temperature decreases. They pointed out that the regularity of those atmospheric oscillations and disturbances is even more regular than that seen in middle-latitude weather systems on Earth.

At last, Fig. 4 is composed by two panels: at the left, the panel presenting the modulus and at the right, the phase angle of the correlation between the pressure (in hPa) and temperature (in °C) data. The purpose is to obtain a correspondence analysis between the signal features.

Evaluated by the modulus and phase of the correlation between the pressure and temperature data, the diurnal and semi-diurnal cycles are also significant to the interpretation, estimated with value about or higher than 36% of the determination coefficient (square of correlation coefficient). The results of the phase correlation in the diurnal cycle are not evident, which indicates that they are not necessarily in phase or anti-phase. However, there is approximately anti-correlation in the scales larger that 1.5 SOL (Fig. 4, right). These scales present a high determination coefficient, i.e., more than 64% (Fig. 4, left). This behavior indicates that only in these scales, the increase in the pressure seems to be strongly associated with the decrease in temperature.

5 Summary and Conclusions

We revisited the pressure and temperature data from Viking Lander Meteorological Experiment datasets, onboard the VL–1, for Mars northern summer, fall, and winter by using signal analysis based on wavelet transform techniques. Even with data gaps, the pressure fluctuations from SOL 1 up to SOL 147 are characterized by minimum SOL-to-SOL variation. After that interval, the amplitude of pressure has increased as a result of the progress of the season.

Diurnal temperature variation appeared to be controlled by atmospheric content: the temperature decreases as the particulate concentration increases. This relationship is linked to seasonality, especially during the summer in the northern hemisphere, when dust storms may occur. In general, these dust storms usually affect the diurnal cycle

Fig. 4 Correlation by scale between pressure and temperature data. The correlation modulus (left panel) and the correlation phase angle (right panel)
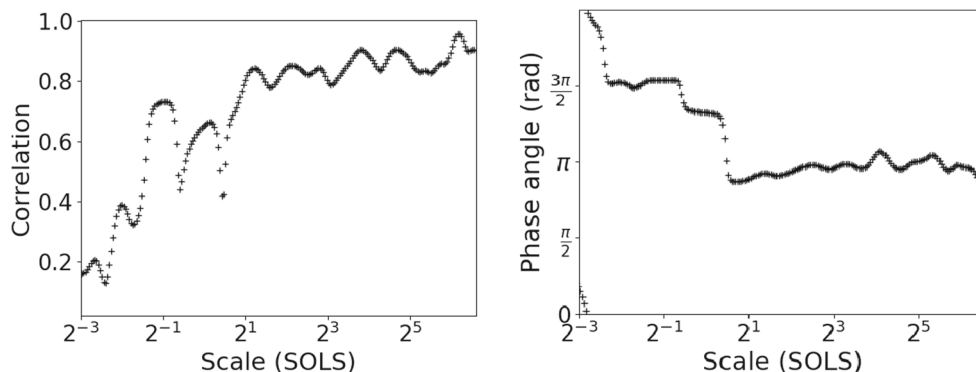
behavior of temperature and pressure in different forms. They intensify the cycle in temperature and reduce the cycle in pressure. Moreover, the semi-diurnal cycle interferes less in pressure than in temperature. This non-stationary behavior affects the global spectrum scale distribution.

From the examination of the multiscale analysis, we observed that the pressure data show evident periods, from Martian-hours to SOLS. It is possible to see diurnal (1 SOL) and semi-diurnal (0.5 SOL), as well as the periodicities as 2, 4, and 8 SOLS. Carr [4] mentions that during the Viking lander missions, the storms pass regularly on a roughly 3-day cycle. We can see that the pressure showed approximately 200 SOLS with a well-defined regime for the diurnal cycle in the pressure. However, around the SOLS $170 - 190$, there has been the onset of apparent global disturbance for more extended periods.

Considering the work of Tillman et al. [19], there was a global disturbance after SOL 200, in the pressure data, culminating around SOL 210. It was related to the first global dust storm detected on Martian surface. The wavelet methodology adopted by us allows detecting the beginning of the dust storm disturbance in advance, around the SOLS $170 - 190$.

We can also see that near the SOL 300 despite the diurnal cycles being sharp and well defined, there is an increase in fluctuations. Snyder [18] presented that around the winter solstice, SOL 300, there was a second global dust storm that can be responsible for that behavior. As our last comment, we would like to point out that the methods used in this work can be applied to other planetary science datasets by its potential to highlight time-scale signal features.

References

1. A.L. Albee, R.E. Arvidson, F. Palluconi, T. Thorpe, Overview of the mars global surveyor mission. J. Geophys. Res. **106**, 23,291–23,316 (2001). https://doi.org/10.1029/2000JE001306
2. J.P. Antoine, R. Murenzi, P. Vandergheynst, S.T. Ali, Two-dimensional wavelets and their relatives. Cambridge (2008)
3. N. Barlow, Mars: An Introduction to its Interior, Surface and Atmosphere (2008)
4. M.H. Carr, *The surface of mars* (Cambridge University press, Cambridge, 2006)
5. M.O. Domingues, O. Mendes, A.M. Costa, On wavelet techniques in atmospheric sciences. Adv. Space Res. **35**(5), 831–842 (2005)
6. F. Forget, F. Costard, P. Lognonne, Planet Mars Story of another world. Spring (2008)
7. P. Frick, S.L. Baliunas, D. Galyagin, D. Sokoloff, W. Soon, Wavelet analysis of stellar chromospheric activity variations. Astrophys. J. **483**(1), 426 (1997). http://stacks.iop.org/0004-637X/483/i=1/a=426
8. P. Frick, R. Beck, E. Berkhuijsen, I. Patrickeyev, Scaling and correlation analysis of galactic images. Mon. Not. R. Astron. Soc. **327**(4), 1145–1157 (2001). https://doi.org/10.1046/j.1365-8711.2001.04812.x
9. P. Frick, A. Grossmann, P. Tchamitchian, Wavelet analysis of signals with gaps. J. Math. Phys. **39**(8), 4091–4107 (1998). https://doi.org/10.1063/1.532485
10. P.J. Gierasch, Martian dust storms. Rev. Geophys. Space Phys. **12**, 730–734 (1974). https://doi.org/10.1029/RG012i004p00730
11. S.L. Hess, R.M. Henry, C.B. Leovy, J.L. Mitchell, J.A. Ryan, J.E. Tillman, Early meteorological results from the Viking 2 Lander. Science **194**, 1352 (1976a). https://doi.org/10.1126/science.194.4271.1352
12. S.L. Hess, R.M. Henry, C.B. Leovy, J.A. Ryan, J.E. Tillman, Meteorological results from the surface of Mars - Viking 1 and 2. J. Geophys. Res. **82**, 4559–4574 (1977). https://doi.org/10.1029/JS082i028p04559
13. S.L. Hess, R.M. Henry, C.B. Leovy, J.A. Ryan, J.E. Tillman, T.E. Chamberlain, H.L. Cole, R.G. Dutton, G.C. Greene, W.E. Simon, J.L. Mitchell, Mars climatology from Viking 1 after 20 sols. Science **194**, 78–81 (1976b). https://doi.org/10.1126/science.194.4260.78
14. S.L. Hess, J.A. Ryan, J.E. Tillman, R.M. Henry, C.B. Leovy, The annual cycle of pressure on Mars measured by Viking Landers 1 and 2. Geophys. Res. Lett. **7**, 197–200 (1980). https://doi.org/10.1029/GL007i003p00197
15. L.A. Magrini, M.O. Domingues, O. Mendes, On the effects of gaps and uses of approximation functions on the time-scale signal analysis: a case study based on space geophysical events. Braz. J. Phys. **47**(2), 167–181 (2017). https://doi.org/10.1007/s13538-017-0486-z
16. T.A. Mutch, S.U. Grenander, K.L. Jones, W. Patterson, R.E. Arvidson, E.A. Guinness, P. Avrin, C.E. Carlston, A.B. Binder, C. Sagan, E.W. Dunham, P.L. Fox, D.C. Pieri, F.O. Huck, C.W. Rowland, G.R. Taylor, S.D. Wall, R. Kahn, E.C. Levinthal, S. Liebes Jr., R.B. Tucker, E.C. Morris, J.B. Pollack, R.S. Saunders, M.R. Wolf, The surface of Mars - The view from the Viking 2 Lander. Science **194**, 1277–1283 (1976). https://doi.org/10.1126/science.194.4271.1277
17. J.A. Ryan, R.M. Henry, S.L. Hess, C.B. Leovy, J.E. Tillman, C. Walcek, Mars meteorology - Three seasons at the surface. Geophys. Res. Lett. **5**, 715–718 (1978). https://doi.org/10.1029/GL005i008p00715
18. C.W. Snyder, The planet Mars as seen at the end of the Viking mission. J. Geophys. Res. **84**, 8487–8519 (1979). https://doi.org/10.1029/JB084iB14p08487
19. J.E. Tillman, R.M. Henry, S.L. Hess, Frontal systems during passage of the martian north polar HOOD over the Viking Lander 2 site prior to the first 1977 dust storm. J. Geophys. Res. **84**, 2947–2955 (1979). https://doi.org/10.1029/JB084iB06p02947
20. N. Venkateswara Rao, N. Balan, A.K. Patra, Solar rotation effects on the Martian ionosphere. J. Geophys. Res. Space Phys. **119**, 6612–6622 (2014). https://doi.org/10.1002/2014JA019894
21. R.W. Zurek, Martian great dust storms - an update. Icarus **50**, 288–310 (1982). https://doi.org/10.1016/0019-1035(82)90127-0
22. R.W. Zurek, J.R. Barnes, R.M. Haberle, J.B. Pollack, J.E. Tillman, C.B. Leovy, Dynamics of the atmosphere of Mars, pp 835–933 (1992)